PAPER

Check for updates

A three-dimensional ZnO/TUD-1 nanocomposite-based multifunctional sensor for humidity detection and wastewater remediation

Aryan Boora,[a] Surender Duhan, ID *[a] Bhavna Rohilla,[a] Priya Malik,[a] Supriya Sehrawat,[a] M. S. Goyat, ID [bc] Yogendra Kumar Mishra ID [c] and Vinod Kumar[d]

This study explores the multifunctional applications of hydrothermally derived 3D (x-ZnO)/TUD-1 nanocomposites (with x = 0, 1, 5, 10, 15%). The fabrication process involves the integration of ZnO nanoparticles into a 3D sponge-like mesoporous TUD-1 host matrix (mesoporous silicate), resulting in a synergistic material with enhanced sensing and adsorption capabilities. The findings reveal the unique behaviour of resistance variation within the nanocomposites over a wide range of relative humidity (11–98%). The nanocomposite with x = 10% shows a 4-fold magnitude change in resistance with response and recovery times of 11 and 9 s respectively. In addition to the sensing capabilities, the nanocomposite was also optimized for photocatalytic activity. The nanocomposite exhibited a superior absorption efficiency of up to 89% for RB (Rose Bengal) dye degradation when confronted with UV (ultraviolet) light as compared to TUD-1 which shows only 52% adsorption efficiency. This multifunctional sensor offers a holistic approach to managing moisture-rich environments and simultaneous wastewater treatment, presenting a valuable contribution to sustainable and efficient environmental monitoring applications.

1. Introduction

Humidity sensing is a fundamental component of numerous applications across diverse industries, encompassing environmental monitoring, industrial automation, healthcare, and consumer electronics.[1] The uprising of more precise and reliable humidity sensors continues to be a critical pursuit, driven by the ever-increasing demand for more accurate, precise environmental data and enhanced control systems.[2] In this context, mesoporous materials have emerged as a promising avenue for advancement in humidity sensing technologies. TUD-1, renowned for its highly disordered and tuneable porous structure, has gained prominence in the realm of materials science and sensor development.[3–5] The concept of resistance-based humidity sensors hinges on the electrical properties of the sensing material, as the RH of the surrounding environment changes, and the electrical conductivity of the sensing material is altered.[6–8] This change in conductivity is harnessed to provide a quantitative measure of humidity.

The highly porous structure of TUD-1 beholds a large surface area for moisture adsorption and also facilitates the diffusion of moisture through its interconnected porous channels.[9,10] TUD-1 with ZnO introduces a novel synergy to its original properties. This structural advantage enhances the sensor's response time and sensitivity.[11] ZnO being an n-type semiconducting material of band gap 3.3 eV imparts high conductivity and responsiveness to changes in humidity levels. This innovative approach seeks to improve some of the difficulties linked with conventional humidity sensors including large response times and limited sensitivity.[12–14] By combining the structural benefits of mesoporous materials like TUD-1 with the sensing ability of ZnO, the developed sensor not only performs exceptionally well but also offers improved reliability and durability over a time domain with minimal hysteresis.[15–19]

In this investigation, we delve into the intricate details of the sensor with cheap fabrication and ease of utility. The sensor exhibits rapid response and recovery times of 11 and 9 s, demonstrating a remarkable four-fold magnitude change in resistance. ZnO hybridised with mesoporous TUD-1 significantly increases the active sites, facilitating greater hydronium ion interaction with the sensor.[17,19] As a result, the sensor becomes highly sensitive to changes in the surrounding environment. The sensor was found to be more selective to the humidity

[a] *Advanced Sensors Lab, Department of Physics, Deenbandhu Chhotu Ram University of Science and Technology, Murthal, Sonepat-131039, Haryana, India. E-mail: surender6561@gmail.com*

[b] *Department of Applied Science, School of Engineering, University of Petroleum and Energy Studies, Dehradun, 248007, Uttarakhand, India*

[c] *Mads Clausen Institute, NanoSYD, University of Southern Denmark (SDU), Denmark*

[d] *Nanomagnetic Research Laboratory, Department of Physics, Netaji Subhas University of Technology, Dwarka, New Delhi-110078, India*

sensing with a sensor response of 98% as compared to other laboratory gases[20,21] and was tested for stability over a time domain of 24 days where the sensor showed almost stable resistance when exposed to varying humidity environments.[22–25] In addition, the photocatalytic efficiency was improved by 88% under UV exposure due to the synergistic effects of the material as it allows for more efficient utilization of light energy.[18,23] The presence of ZnO hybridised with mesoporous silicate promotes effective charge separation and migration, reducing recombination rates and enhancing the generation of reactive species, leading to improved photocatalytic performance.[25–31]

2. Experimental

2.1 Materials

In order to obtain porous structured TUD-1 and 3D (x-ZnO)/TUD-1 nanocomposites, tetraethyl orthosilicate (TEOS) was used as a biocompatible silica source and was procured from Sigma Aldrich. For the addition of zinc in the matrix, zinc nitrate hexahydrate ($Zn(NO_3)_2 \cdot 6H_2O$) salt was used and was acquired from Alfa Aesar, while tetraethylammonium hydroxide (TEAOH) was utilized as a reagent to establish the required basic reaction environment and was obtained from Sigma Aldrich. Triethanolamine (TEA), assay 97% and double distilled water were procured from SRL Chemical Labs.

2.2 3D (x-ZnO)/TUD-1 nanocomposite preparation

3D (x-ZnO)/TUD-1 nanocomposites (x = 0, 1, 5, 10, 15%) were synthesized using a one-pot hydrothermal technique. In a typical synthesis of pure TUD-1, 13.2 g of triethanolamine was diluted in 8 mL of deionized water and added to 18.4 g of tetraethyl orthosilicate with the help of a dropper under vigorous stirring. After 40 min, 15.8 g of TEAOH was introduced drop by drop, and the solution was stirred for 3 h at 35 °C to obtain a clear solution. The homogeneous transparent solution was left for aging at room temperature for 1 day; subsequently, the solution was dried in an oven at 100 °C for another 24 h. The resulting brownish solid was subsequently ground, and then it underwent hydrothermal treatment in a 50 mL autoclave at 190 °C, subjected to self-generated pressure, for a duration of 8 h. The solid was then ground once more and subjected to calcination at 550 °C for 9 h, at a heating rate of 1° min⁻¹. Nanocomposites with various zinc oxide compositions were synthesized following a similar procedure as discussed above with the addition of required amounts of zinc nitrate hexahydrate salt solutions to the initially diluted TEA.[5–8]

2.3 Characterization

Powder X-ray diffraction patterns were obtained using an Empyrean X-ray diffractometer (50 kV and 50 mA) equipped with a monochromator utilizing Cu Kα radiation (λ = 0.158 nm) with the angle varying from 20° to 80°. For small angle X-ray scattering patterns, Anton Par SAXS 2.0 was utilised to determine the mesoporous nature at low angles ranging from 0 to 4°. Surface area measurements and pore volume determinations for the nanocomposites were conducted at 78 K with a Microtrac MRB BELSORP MAX sorption analyser. Prior to these measurements, samples were exposed to a pre-heat temperature of 473 K for 24 h. Pore size distributions were ascertained through adsorption branching, using the Barrett–Joyner–Halenda model. The Brunauer–Emmett–Teller (BET) method was used to determine the surface area, and pore volumes were determined with the help of a T-plot.

UV DRS spectra were recorded under static conditions using a Shimadzu UV-3600i plus spectrophotometer. Field-emission scanning electron microscopy was conducted at 15 kV on a Zeiss Gemini SEM 500 field emission type microscope. To prevent charging effects, the nanocomposite surfaces were coated with gold. In order to determine the chemical composition of the prepared specimens, energy dispersive X-ray (EDX) analysis was conducted. Transmission electron microscopy (HRTEM) was carried out with a Tecnai F30 S-Twin electron microscope operating at 200 kV. Specified samples were deposited on carbon coated copper grids by immersing the copper grid in a suspension of each finely ground sample that had been solvated in acetone, and then the grid was dried under ambient conditions.

2.4 RH sensor fabrication

The fabrication of sensors using the mesoporous ZnO/TUD-1 powder deposition method *via* drop casting involves a series of precise steps. Initially, 5 Ag–Pd interdigitated electrodes (IDE) were washed with distilled water and ultrasonicated in acetone.[14] Finally, the substrate was heated in an oven at 90 °C to evaporate the impurities and any kind of contamination. In this process, the prepared nanocomposites were initially ground and then a viscous paste in ethanol with a ratio of 1 : 5 was carefully prepared.[15] This slurry paste was then deposited onto the Ag–Pd electrode using a micropipette.[3,4] After the deposition, the electrodes were left to dry at 100 °C for 4 h. The solvent was allowed to evaporate, leaving behind a uniform layer of mesoporous ZnO/TUD-1 nanocomposite on the electrode surface as shown in Fig. 1.

The environment with ramping relative humidity RH (11–98%) was achieved by preparing saturated salt solutions inside the airtight chambers. In this experiment, the utilised salt solutions were prepared with lithium chloride (LiCl), magnesium chloride ($MgCl_2 \cdot 6H_2O$), magnesium nitrate ($MgNO_3)_2 \cdot 4H_2O$), sodium chloride (NaCl), potassium chloride (KCl) and potassium sulphate (K_2SO_4).[4] The enclosed chambers with prepared solutions were left overnight to achieve the equilibrium for precise measurement. Then the response of the fabricated sensor was analysed, the material deposited substrates were exposed to the ambient RH condition with salt solutions and the corresponding change in the resistance was monitored consecutively.[14–17]

2.5 Photocatalytic activity

The catalytic performance of the prepared nanocomposites was assessed by examining the absorbance spectra within the range of 200–800 nm. This analysis involved a model RB dye solution exposed to visible light as shown in Fig. 2(a). Typically, 5 mg of
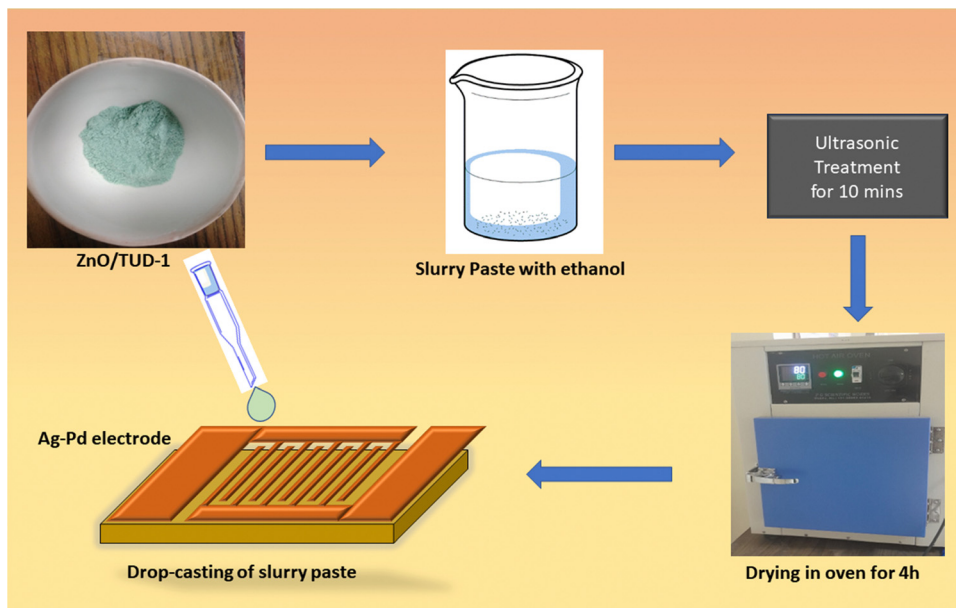
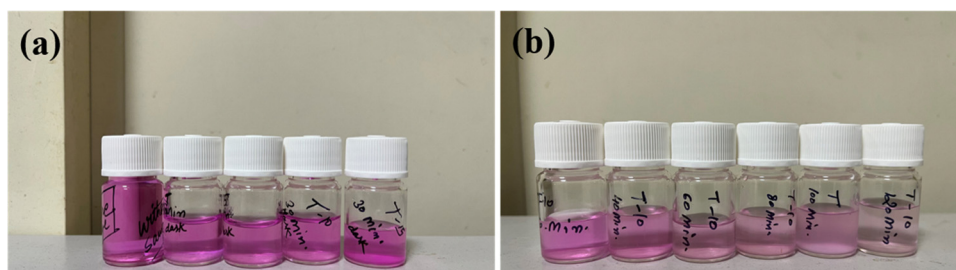**Fig. 1** Fabrication of the ZnO/TUD-1 sensor *via* drop casting.

Fig. 2 (a) ZnO/TUD-1 nanocomposites after attaining equilibrium of adsorption in a dark chamber for 30 min and (b) RB dye degradation samples collected from time (T) = 0 to 120 min.

the catalyst was dissolved in 50 mL of the RB dye solution and stirring was continued for 30 min in a dark chamber to establish an adsorption–desorption equilibrium phase between the dye and the catalyst.[28,29] A 300 W xenon lamp served as the light source. Small 2 mL aliquots of the solution were periodically collected at 20 min intervals and centrifuged in triplicate at 5000 rpm for 5 min. The nanocomposites were then filtered through a 0.2 μm nylon membrane.[29–31] To gain a deeper understanding of the catalyst and light's influence on the photocatalytic process, the samples were collected at regular time intervals of 20 min as shown in Fig. 2(b).

3. Experimental results

3.1 SAXS

The initial structural assessment of the prepared nanocomposites was established using SAXS. In Fig. 3, a clearly sharp defined peak was observed at an angle of 0.89° which confirms the mesoporous nature of TUD-1, characterized by its disordered, sponge-like structure.[32–34] Remarkably, as the concentration of ZnO nanoparticles increased, the peak shifted slightly
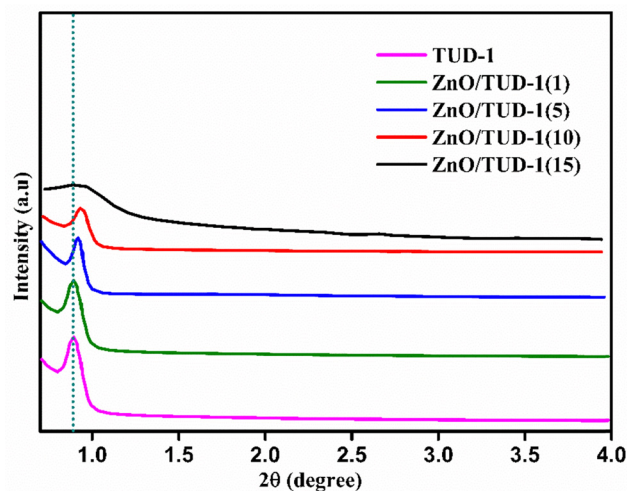

Fig. 3 SAXS patterns confirming the amorphous nature of ZnO/TUD-1 nanocomposites.

to 0.90°. This shift was attributed to the development of the crystalline phase of zinc oxide nanoparticles within the

siliceous host matrix. This crystalline phase leads to a decrease in the lattice spacing of nanoparticles.

However, at higher concentrations of zinc nanoparticles, emergence of a broad, flat band was observed signifying the disrupted nature of the silica matrix which shows the drop in porosity of the material. This drop in porosity might be attributed to the pore filling effect caused by the formation of large sized zinc oxide structures. Thus, the appearance of a shift in SAXS indicates a change in the nanoscale structure of the composite material.

3.2 WAXRD

Fig. 4 shows the wide-angle X-ray diffraction plots from $2\theta = 20°$–$80°$ performed at a scan rate of $1°$ per minute. The amorphous nature of the pristine TUD-1 material is confirmed from the silica hump present at $22°$ which is due to its worm-hole structure. With the addition of zinc, sharp peaks were also observed along with the silica hump confirming the growth of the polycrystalline phase of ZnO inside the amorphous silic-eous material. This has also been confirmed from the SAXS pattern (Fig. 3). But with a high loading of zinc oxide, sharp peaks with very high intensity are observed at $31.78°$ (100), $34.4°$ (002), $36.2°$ (101), $47.56°$ (102), $56.77°$ (110), $62.9°$ (103), $66.40°$ (200), $68.00°$ (112), and $69.09°$ (201) almost disturbing the amorphous nature of TUD-1.[30] The indexing of these planes has been verified using the standard reference (JCPDS: 36-1451) corresponding to zinc oxide species. The obtained crystallite size (D) was 25.31 nm for the most intense peak corresponding to the (101) plane calculated from the Scherrer formula presented in eqn (1).

$$D = \frac{K\lambda}{\beta \cos\theta} \quad (1)$$

where K represents the Scherrer constant with a value of 0.9, λ is the wavelength of CuKα (1.54 Å), β is the FWHM of the most intense peak and θ is the corresponding Bragg's angle.
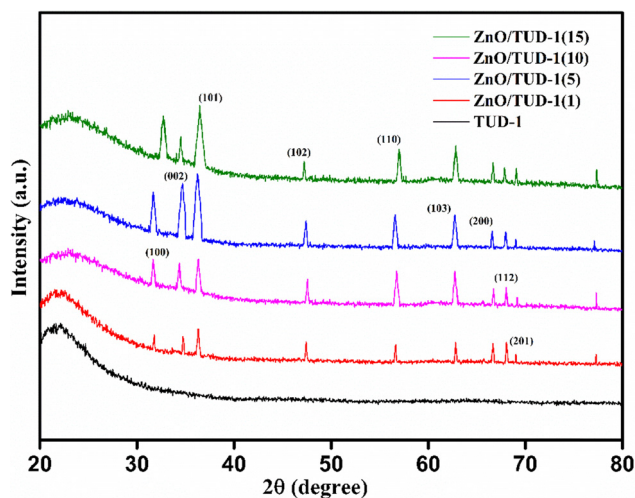

Fig. 4 WAXRD pattern confirming the existence of polycrystalline nature of ZnO incorporated amorphous TUD-1.

The interplanar spacing was determined to be 0.28 nm and 0.26 nm for the (100) and (002) planes, respectively. This has been evaluated using eqn (2) corresponding to the wurtzite hexagonal zinc oxide structure as given below[35]

$$d_{hkl} = \frac{1}{\sqrt{4(h^2 + k^2 + hk)/3a^2 + l^2/c^2}} \quad (2)$$

where a and c are the lattice parameters.

$$a = \frac{\lambda}{\sqrt{3}\sin\theta_{100}} \quad \text{and} \quad c = \frac{\lambda}{\sin\theta_{002}} \quad (3)$$

3.3 FESEM-EDX

The surface morphology was assessed using FESEM, revealing distinct features. In Fig. 5(a and b), pristine TUD-1 displayed flake-like structures of non-uniform sizes at a resolution of 20 μm.[36] However, at a higher resolution of 200 nm, the micrographs revealed silica particles with a fluffy, cotton-like structure. Fig. 5(c) displays the EDX spectra of TUD-1, indicating the existence of pure silica and oxygen peaks, affirming the material's purity. Fig. 5(d) presents a similar flake-like structure of zinc-doped silica at a resolution of 20 μm, showing minimal differentiation.[37] However, when observed at a higher resolution of 200 nm as shown in Fig. 5(e), the formation of some zinc oxide nanowires and irregularly shaped structures becomes evident. Additionally, some zinc oxide nanoparticles are visible within the hollow region, as well as across the surface of the siliceous matrix, as highlighted in the rectangular boxes.

In Fig. 5(f), we observe a distinct, sharp peak at 1 keV, accompanied by a minor hump at 8.5 keV, which justifies the presence of zinc species.[38,39] This observation confirms the successful integration of zinc oxide within the siliceous matrix. Notably, two additional peaks appear at approximately 0.28 keV and 2.1 keV. These peaks are a result of the carbon coatings and gold plating that were strategically applied to improve conductivity and mitigate charging effects during the spectral analysis.

3.4 HRTEM

The HRTEM micrographs depicted in Fig. 6(a) showcase the pristine TUD-1 in its pure form. These micrographs reveal the presence of visible pores and tunnels arranged in structures resembling tiny cotton balls, intricately interconnected with one another.[37] These findings align with the observations in the FESEM micrographs. Importantly, these pores furnish a substantial surface area and serve as active adsorption sites, facilitating the smooth transport of hydronium ions through the channels.[4] In Fig. 6(b), we observe hexagonally shaped zinc oxide nanoparticles clearly embedded within the porous silica network. These nanoparticles are notably distributed within the confined spaces of the silica matrix, with an average particle size of 11 nm.[40,41] The inset shows a closer perspective, highlighting the interplanar spacing of these zinc oxide nanoparticles.

The SAED pattern of pristine TUD-1 in Fig. 6(c) reveals the absence of diffraction rings, indicating its amorphous nature.
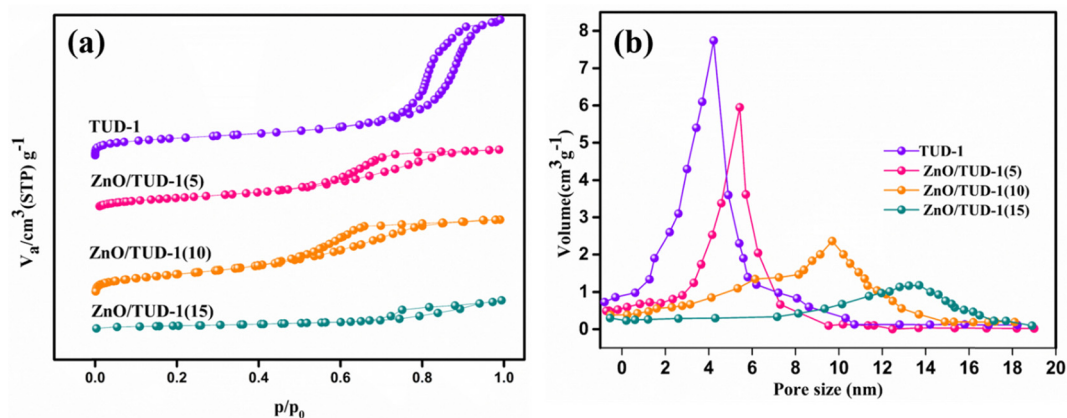
Fig. 5 (a)–(c) FESEM with EDX micrographs showing the amorphous nature of TUD-1 and (d)–(f) x = 10%.

Fig. 6 HRTEM micrographs of (a) TUD-1 and (b) zinc oxide structure embedded in the TUD-1 matrix. SAED pattern of (c) amorphous TUD-1 and (d) ZnO/TUD-1(10).

In contrast, Fig. 6(d) presents clear and vivid diffraction rings, providing unequivocal evidence for the presence of fine, nano-sized ZnO particles.

3.5 BET

Fig. 7(a) presents N_2 adsorption–desorption isotherms for the synthesized samples. Following degassing at 200 °C for 24 h,

the nanocomposites underwent N_2 gas sorption analysis and the specific surface area and pore diameter were determined. ZnO/TUD-1 nanocomposites exhibit type IV isotherms and H2 hysteresis loops in the N_2 physisorption isotherms at 77 K. This reflects their retained disordered mesoporous structural properties with a very slight decrease in retentivity curve.[3,4,14] However, for x = 15%, the hysteresis loop is

Fig. 7 (a) N$_2$ adsorption–desorption isotherms and (b) pore size distribution curves of the prepared ZnO/TUD-1(x) nanocomposites.

Table 1 Structural and surface properties of the ZnO/TUD-1(x) nanocomposites

Specimen	S_{BET} (m^2 g^{-1})	Pore volume V_P (cm^3 g^{-1})	Pore diameter D_P (nm)
TUD-1	743	0.87	4.2
ZnO/TUD-1(5%)	678	0.74	5.42
ZnO/TUD-1(10%)	629	0.62	9.7
ZnO/TUD-1(15%)	451	0.45	13.6

transformed to a vertical H1 pattern. This transformation indicates a reduction in mesoporous characteristics, attributed to pore constriction.[27,42]

Pristine TUD-1 exhibited the highest specific surface area of 743 m^2 g^{-1}, primarily attributed to the presence of narrow-sized pores measuring 4.2 nm within its spongy siliceous structure. The impact of zinc oxide on the variation in pore size for different compositions is depicted in Fig. 7(b). However, as the concentration of zinc oxide increased, the specific surface area decreased to 451 m^2 g^{-1} due to the widening of pores to 13.6 nm, as discussed in Table 1. This reduction in surface area was primarily caused by the formation of larger crystalline particles of zinc oxide at x = 15%, leading to the obstruction of pores within the silica matrix.

3.6 Diffuse reflectance spectroscopy

The UV diffuse reflectance spectra shown in Fig. 8(a) were used for the investigation of optical properties. For pristine silica, absorption bands appeared at 231 and 290 nm, while the zinc oxide nanocomposite exhibited an absorption band at 383 nm.[43] In Fig. 8(b), the observed band gaps from Kubelka–Munk and Tauc plots for pristine TUD-1 and x = 10, 15% are depicted. The pristine silica matrix, being an insulator, displayed a wide band gap of 5.3 eV, with a noticeable kink at 4.1 eV attributed to the absorption band observed at 288 nm in the reflectance spectrum.

In contrast, the wide band gaps of zinc oxide and silica nanocomposites were modified to 3.23 and 3.3 eV, respectively, for x = 10% and 15%. This alteration can be attributed to the redshift of absorption bands in silica species, induced by the presence of zinc oxide nanoparticles within the porous silica network domains.[44]

4. Humidity sensing and photocatalytic properties

4.1 Humidity sensing

After careful material deposition as discussed in Section 2.4, the substrates were exposed to varying relative humidity (RH) conditions, revealing a notable decrease in resistance as RH
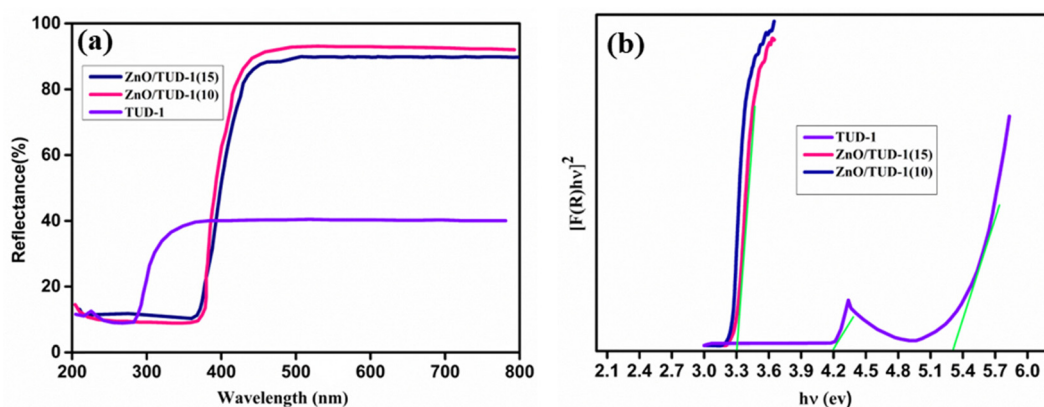

Fig. 8 (a) Diffuse reflectance spectrum and (b) band gap evaluation using Tauc plot for the ZnO/TUD-1(x) nanocomposites.
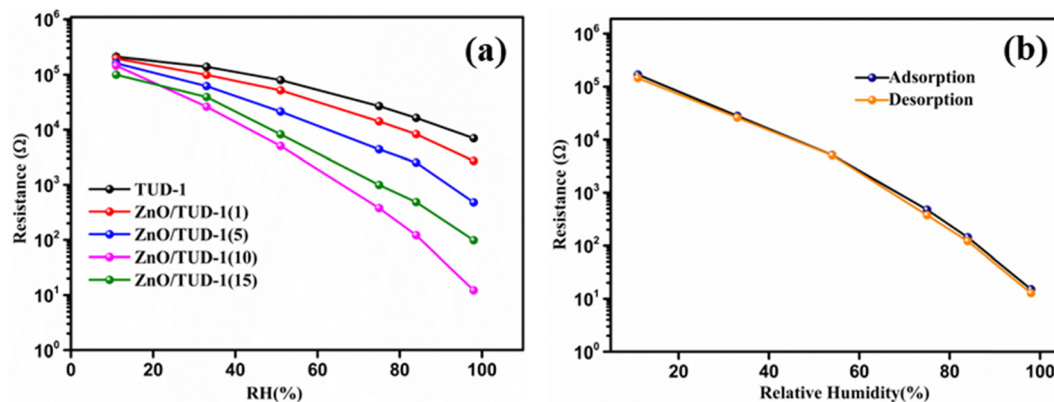
Fig. 9 (a) Resistance *vs.* RH curves for the as-synthesized ZnO/TUD-1(*x*) nanocomposites and (b) hysteresis curve for ZnO/TUD-1(10).

levels increased as shown in Fig. 9(a). In the case of pristine TUD-1, a modest change of less than one order of magnitude in resistance was observed across the entire RH range of 11–98%. However, as the concentration of ZnO within the siliceous material increased, a sharp and significant decline in resistance, amounting to a four-order magnitude change, was evident in the ZnO/TUD-1(10) sensor.[3,4] This phenomenon of improved conductivity can be attributed to the uniform distribution of zinc oxide nanoparticles within the silica matrix, as confirmed by FESEM and HRTEM analysis. ZnO, being a semiconducting material, acts as a sensitizing agent when incorporated into the mesoporous structure of TUD-1.[10] The interactions between ZnO and mesoporous silica nanoparticles further enhance the sensor's capacity to adsorb and desorb water molecules, resulting in rapid sensitivity and a more pronounced change in resistance in response to fluctuations in humidity levels.

Nevertheless, a shift in the trend is noticeable at higher ZnO concentrations within silica, exemplified by the ZnO/TUD-1(10) sensor. In contrast to the earlier findings of improved conductivity, a reduction in conductivity becomes apparent.[14–19] This deviation from previous observations could be attributed to the pore constriction and the formation of larger nanoparticles, as evidenced in the BET sorption isotherms.[14] The humidity

sensor based on the mesoporous ZnO/TUD-1 nanocomposite demonstrates remarkable performance with minimal hysteresis (Fig. 9(b)), signifying its ability to consistently deliver precise humidity measurements across multiple cycles.

Fig. 10(a) shows the repeated response and recovery cycles of the sensor revealing its exceptional performance in maintaining nearly identical resistance changes over three consecutive cycles.

Experimental results show that it exhibited a rapid response time of 11 s, swiftly reacting to changes in its environment along with its swift recovery time of 9 s, efficiently returning to its initial state with altered RH as shown in Fig. 10(b). The sensor was found to be much more efficient due to fine adsorption and desorption of water molecules inside the porous channels present in the ZnO/TUD-1 nanocomposite. This quick and consistent response and recovery behaviour highlights the sensor's effectiveness, making it a valuable asset in applications where rapid and reliable measurements are essential.[15–17]

A rigorous stability test was executed for the most promising specimen, spanning a 24-day period across all RH conditions, as depicted in Fig. 11. Remarkably, the sensor exhibited steady resistance values without any discernible fluctuations under specific RH conditions. This extended time-domain assessment
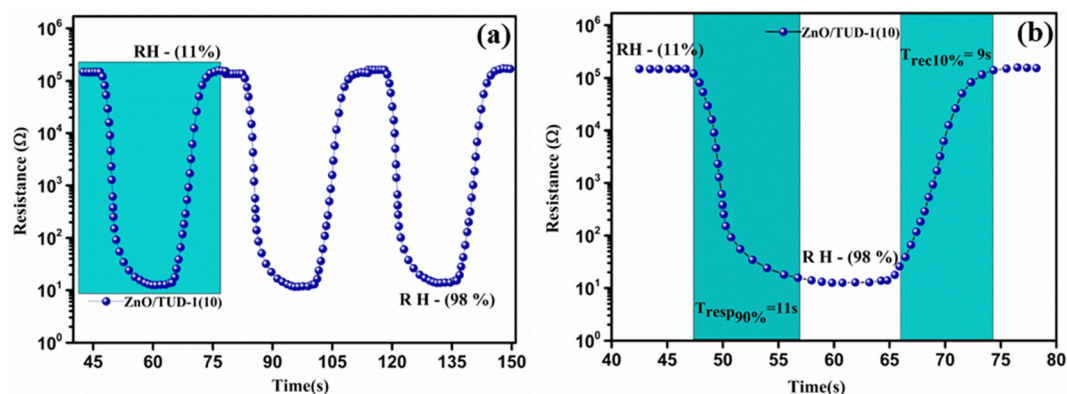

Fig. 10 (a) Repeated response and recovery cycles of the ZnO/TUD-1(10) sensor and (b) average response and recovery curve for the ZnO/TUD-1(10) sensor.
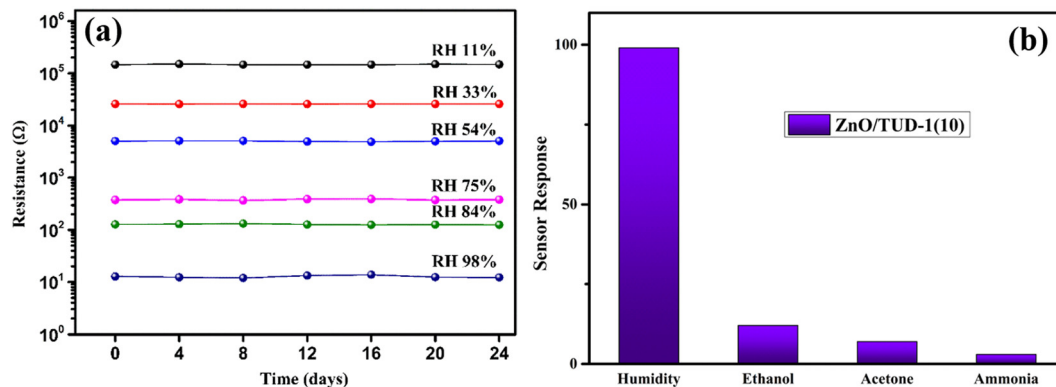
Fig. 11 (a) ZnO/TUD-1(10) sensor showing excellent stability over a time domain and (b) selectivity of the sensor to various gases.

aimed to verify the sensor's reliability and consistency over an extended period, ensuring its suitability for long-term and reliable measurements in various applications.[16]

4.2 Selectivity of the sensor

Selectivity refers to the capacity of the sensor to react basically to just a single chemical component or compound within the sight of different species. The sensor exhibits remarkable precision in detecting humidity levels amidst various environmental conditions, showcasing its ability to distinguish the moisture content from other factors accurately.[20,21] This capability is essential for applications requiring precise humidity monitoring, such as climate control systems, agricultural set-ups, and industrial processes. Additionally, the sensor underwent tests for detecting ethanol, acetone, and ammonia but demonstrated greater sensitivity towards humidity with a response of 98% followed by ethanol, acetone and ammonia which show a negligible response.[24,31,50] Fig. 11(b) shows sensor response (R_r) that was evaluated using the following standard equation:

$$R_r = \frac{R_g - R_a}{R_a} \qquad (4)$$

where R_g and R_a refer to the sensor's resistances on exposure to test the gas and ambient air respectively. All the electrical tests and measurements were performed at RT (27 °C).

4.3 State-of-the-art humidity sensors

Modern humidity sensors employ state-of-the-art capacitive or resistive sensing mechanisms, ensuring precise and rapid humidity measurements with remarkable accuracy. The continuous evolution of materials engineering and sensor design contributes to the ongoing enhancement of humidity sensing technologies, catering to a broad spectrum of scientific and industrial needs. Here Table 2 lists state-of-the-art humidity sensors from the literature developed in recent periods of time.

4.4 Light-assisted catalytic analysis

The degradation of RB dye using zinc oxide-doped mesoporous TUD-1 represents a promising avenue in the realm of environmental remediation. Investigation of the adsorption behaviour

of the prepared nanocomposites towards the dye was performed at 28 °C in an isolated environment. The experiment was performed by dissolving the material in 0.5 mg mL^{-1} dye solution.[28] Fig. 12(a) shows a comparative study of the decrease in concentration of dye with time for all the specimens at a regular time interval of 20 min. In the initial phase, the solutions were gently stirred within a dark chamber for a duration of 30 min, without any exposure to light radiation, in order to establish an equilibrium state for the adsorption–desorption phenomenon.[29–31] It's worth noting that a minor level of degradation occurred during this time interval, attributable to the adsorption sites within the porous structure of the mesoporous siliceous matrix. After the initial equilibrium phase, all specimens underwent a comprehensive 120-min evaluation of their photocatalytic performance, with the $x =$ 10% sample demonstrating the highest degree of concentration degradation.

As displayed in Fig. 12(b), a noticeable rise in the degradation percentage is evident with an increase in the quantity of zinc oxide incorporated into pristine silica. This phenomenon arises as a result of synergistic effects, where the exceptional attributes of silica such as its extensive surface area and porous nature, furnish ample adsorption sites for the target molecules to adhere to the catalyst's surface.[32] Zinc oxide, being an n-type semiconducting material, possesses the capability to adsorb photons and generate electron–hole pairs when exposed to light. When introduced into mesoporous silica, heterojunction formation facilitates the effective charge separation. This separation of charges plays a pivotal role in propelling photocatalytic reactions. However, in the case of a very high concentration of zinc oxide loading ($x = 15\%$), the degradation efficiency (η) exhibited a decline as discussed in Table 3.

$$\text{Degradation efficiency}(\eta) = \frac{C_0 - C}{C_0} \times 100\% \qquad (5)$$

where C_0 corresponds to the initial concentration and C is the concentration at irradiation time t.

This observation could be attributed to the reduced surface area and the inadequacy of available adsorption sites for molecules.[29–34] The abundance of zinc oxide nanoparticles within

Table 2 A comparative study of zinc oxide-based resistive sensors

S. no.	Material	Response/recovery time (s)	Substrate used	R.H. (%)	Hysteresis	Cost	Ref.
1.	PVDF/ZnO	30/51	ITO	5–98	—	Medium	45
2.	ZnO	31/15	Ag/Pd	11–95	0.9	Medium	46
3.	TPPNi-ZnO	30/30	Glass	40–85	—	Medium	47
4.	GO/ZnO/PCF	19/28	Al_2O_3	11–97	2.37	High	48
5.	TiO_2/ZnO	18/22	Fork finger	11–95	1.55	Low	49
6.	ZnO/WS_2	74/53	Glass	18–85	—	High	50
7.	Au/ZnO	16/28	Al_2O_3	11–95	3	High	51
8	PVDF/PMMA/ZnO	39/16	Spin coating	31–100	—	High	52
9	PANI/ZnO	85/120	ITO	20–90	—	Medium	53
10	ZnO/TUD-1	11/9	Ag/Pd	11–98	—	Low	Present work
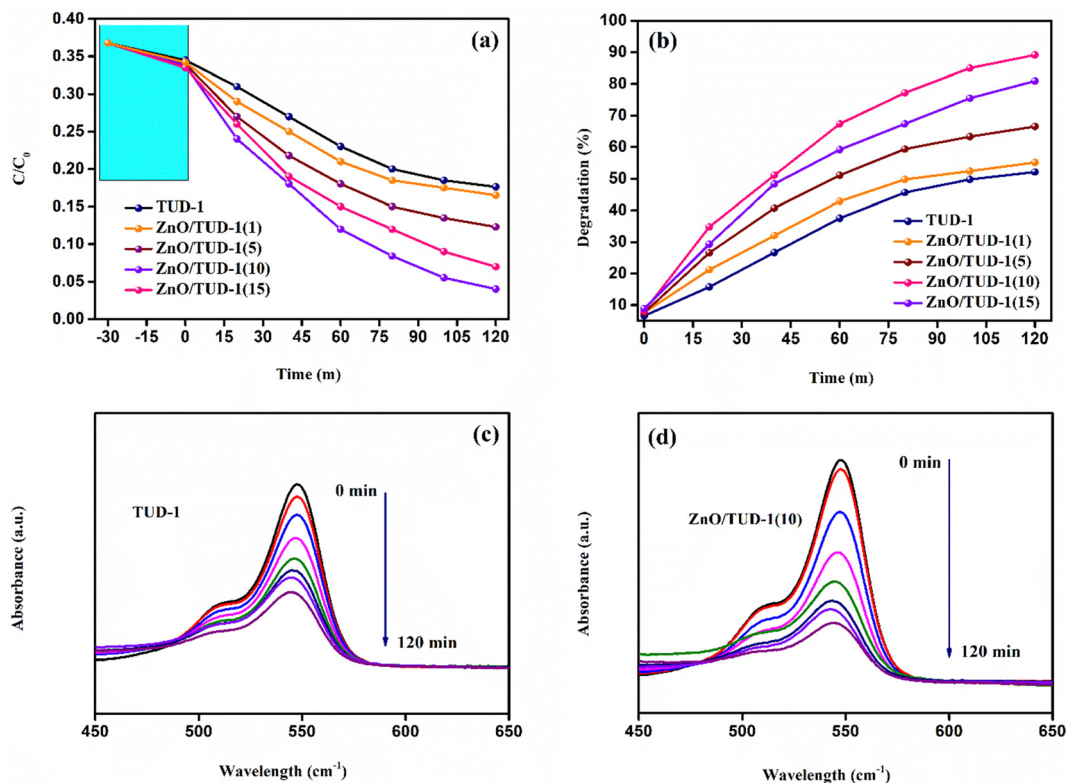
Fig. 12 (a) Decrease in the concentration gradient of RB dye for the synthesized ZnO/TUD-1(x) nanocomposites, (b) degradation efficiency of the nanocomposites, and (c) and (d) the obtained UV absorbance spectra for TUD-1 and ZnO/TUD-1(10) respectively after the degradation process.

Table 3 Degradation efficiency of the ZnO/TUD-1(x) nanocomposites in the dark and in the presence of UV light

Specimen	η in the dark (%)	η in the entire range (%)
TUD-1	6.5	52.17
ZnO/TUD-1(1)	7.0	55.26
ZnO/TUD-1(5)	7.6	66.57
ZnO/TUD-1(10)	8.1	89.13
ZnO/TUD-1(15)	8.9	80.92

the matrix induces pore blockage, ultimately contributing to a decline in photocatalytic activity. Fig. 12(c and d) illustrate the reduction in RB dye intensity, as determined from the absorbance spectrum for specimens with x = 0 and 10%. It is evident from these data that the introduction of zinc oxide

nanoparticles has enhanced the degradation efficiency by 71% when compared to pristine silica.

4.5 Radical detection and reusability of the photocatalyst

A scavenger test was conducted using EDTA (ethylenediamine-tetraacetic acid), benzoquinone, and isopropanol in order to investigate the active intermediate species involved in the photocatalytic degradation process facilitated by the best-performing specimen, ZnO/TUD-1(10). The results revealed hydroxyl radicals (•OH) as the active intermediate species, contributing significantly to the degradation mechanism as shown in Fig. 13(a). Isopropanol, a scavenger for hydroxyl radicals, was introduced into the reaction mixture, resulting in a reduction of the dye degradation efficiency to 41%.
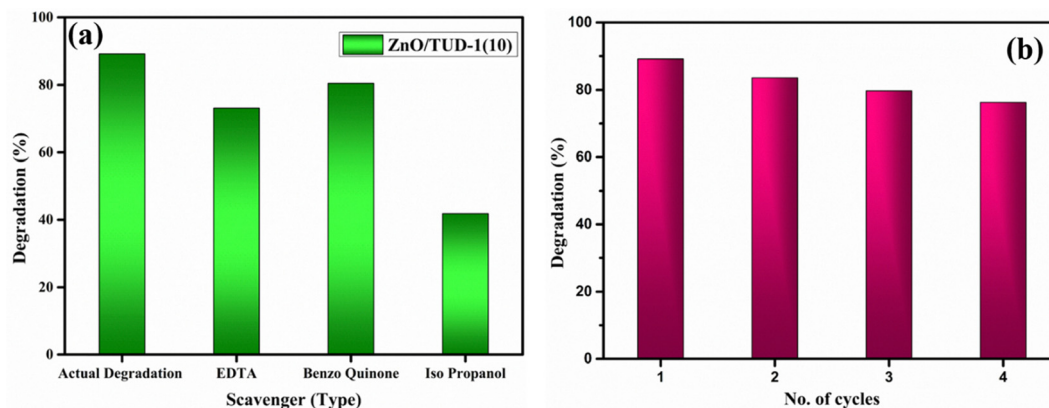
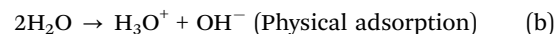**Fig. 13** (a) Scavenger test for ZnO/TUD-1(10) and (b) the reusability test.

This reduction underscores the role of hydroxyl radicals in driving the photocatalytic degradation process of organic dyes which were trapped by the isopropanol scavenger.[54,55] These findings provide valuable insights into the degradation mechanism of ZnO/TUD-1(10) and highlight the importance of hydroxyl radicals as key intermediates in the photocatalytic process.

The reusability of the ZnO/TUD-(10) nanocomposite as a photocatalyst investigated by subjecting it to multiple cycles of filtration and washing has been shown in Fig. 13(b). After being filtered and reused for four cycles, the efficiency of the nanocomposite decreased to 76%, indicating some loss of activity over successive cycles. This decrease could potentially be attributed to the loss of photocatalytic materials during the filtration and washing procedures.[54–56]

5. Grotthuss mechanism

The proposed humidity sensor operates through a sensing mechanism that is enhanced by various factors. The introduction of ZnO nanoparticles into the mesoporous silica matrix increases the number of active sites. At a low relative humidity (RH%), a limited amount of water molecules is adsorbed, constrained by the surface of the ZnO/TUD-1 nanocomposite through a combination of physisorption and chemisorption processes. Initially, water molecules dissociate into OH^- and H^+, chemisorbing onto the composite surface, serving as the primary conduction process at a low RH.[3,4] As RH increases, the quantity of water molecules adsorbed becomes very high, resulting in the continuous formation of both physisorbed and chemisorbed water layers as represented in Fig. 14.

$$H_2O \rightarrow H^+ + OH^- \text{ (Chemical adsorption)} \qquad \text{(a)}$$

$$2H_2O \rightarrow H_3O^+ + OH^- \text{ (Physical adsorption)} \qquad \text{(b)}$$

$$H_3O^+ \rightarrow H_2O + H^+ \qquad \text{(c)}$$

This leads to the production of a significant amount of H_3O^+ ions, accelerating the electrolytic conduction process and
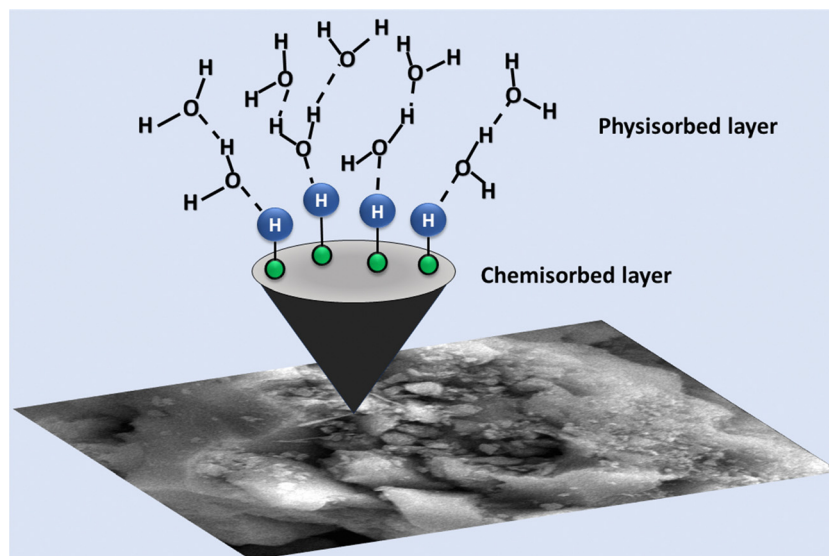

Fig. 14 Schematic representation of proton ion transport in the ZnO/TUD-1 sensor *via* hydronium ions.

enhancing the humidity sensing performance. Ionic conductivity becomes more efficient, causing an increase in electrical response and a substantial decline in the resistance. The electrical response correlates with the number of water molecules adsorbed on the sensing material surface.

Additionally, the incorporation of ZnO nanoparticles into the TUD-1 matrix results in a high free electron density, creating local strong electric fields on the surface of the ZnO/TUD-1 hybrid nanocomposite. This field improves water molecule ionization, particularly on the physisorbed layers and defect sites of the ZnO/TUD-1 nanocomposite, generating H^+ ions on its surface. The ionization process significantly increases from 11–98% RH, resulting in a 4 orders magnitude change in resistance.[57–60]

6. Conclusions

The 3D ZnO/TUD-1 nanocomposite sensor synthesized *via* a hydrothermal approach exhibited exceptional humidity sensing, distinguished by its rapid response and recovery times of 11 and 9 s with minimal hysteresis. The 3D sensor revealed outstanding stability over a time domain with a 4-fold magnitude drop in resistance in the entire range 11–98% RH as compared to a mesoporous silicate host matrix. Structural analysis by SAXS and WAXRD confirmed the influence of ZnO on TUD-1. The large specific surface area of 451 m^2 g^{-1} provides active adsorption sites resulting in enhanced humidity sensing properties. The morphological analysis by FESEM and HRTEM techniques conclusively validated the formation of cloud-like and cotton ball-like structures within the host matrix with a band gap of 3.23 eV. The outcomes of these characteristics showcased a seamless consensus, highlighting the stability and useability of the synthesized material. Additionally, the 88% efficacy in dye degradation accentuates its versatility and promise in addressing environmental concerns such as wastewater treatment and environmental technologies.

Author contributions

In this work, Aryan Boora performed synthesis, collected and analysed the data, optimized the results and wrote the paper. Bhavna Rohilla, Priya Malik, and Supriya Sehrawat revised it to enrich its core intellectual content. M. S. Goyat critically reviewed the study. Surender Duhan and Y. K. Mishra have reviewed and endorsed the final version of the manuscript, accepting responsibility for its accuracy and integrity.

Conflicts of interest

The authors have no conflicts to disclose.

Acknowledgements

References

1 Q. Zhao, Y. Jiang, Z. Duan, Z. Yuan, J. Zha, Z. Wu and Q. Huang, *et al.*, A Nb₂CTₓ/sodium alginate-based composite film with neuron-like network for self-powered humidity sensing, *Chem. Eng. J.*, 2022, **438**, 135588, DOI: **10.1016/j.cej.2022.135588**.

2 S. Sehrawat, S. P. Nehra and S. Duhan, *In situ* hydrothermally derived highly responsive MgO doped mesoporous KIT-6 based novel humidity sensor, *Mater. Res. Innovations*, 2024, **28**(2), 94–105, DOI: **10.1080/14328917.2023.2236846**.

3 B. Rohilla, A. Boora, M. S. Goyat and S. Duhan, Exploring 2D hexagonal WO 3/COK-12 nanostructures for efficient humidity detection, *Mater. Adv.*, 2023, **4**(22), 5785–5796, DOI: **10.1039/D3MA00691C**.

4 A. Boora, S. Duhan and V. Kumar, Novel highly flexible room temperature humidity sensor based on mesoporous NiO/TUD-1 hybrid nanocomposite, *J. Mater. Sci.*, 2023, 1–17, DOI: **10.1007/s10853-023-09013-1**.

5 M. Benaissa, A. M. Alhanash, M. Eissa and M. S. Hamdy, Solvent-free selective hydrogenation of 1,5-cyclooctadiene catalyzed by palladium incorporated TUD-1, *Catal. Commun.*, 2017, **101**, 62–65, DOI: **10.1016/j.catcom.2017.07.026**.

6 M. S. Hamdy, B. M. Al-Shehri, K. S. Al-Namshah and M. Shkir, Synthesis, characterization, and photoluminescence property of Nd–TUD-1, *Luminescence*, 2021, **36**(1), 192–199, DOI: **10.1002/bio.3934**.

7 H. Miao, W. Zhong, H. Yuan, W. Jiang and G. Hu, One-pot synthesis of nitrogen-doped carbons with hierarchically micro-and mesoporous structures for supercapacitors and CO_2 capture, *New J. Chem.*, 2021, **45**(15), 6618–6629, DOI: **10.1039/D0NJ05523A**.

8 A. T. Mubarak, A. M. Alhanash, M. Benaissa, H. H. Hegazy and M. S. Hamdy, In-situ activation of Pd-TUD-1 during the selective reduction of 1,5-cyclooctadiene, *Microporous Mesoporous Mater.*, 2019, **278**, 225–231, DOI: **10.1016/j.micromeso.2018.11.035**.

9 L. Li, T. I. Korányi, B. F. Sels and P. P. Pescarmona, Highly-efficient conversion of glycerol to solketal over heterogeneous Lewis acid catalysts, *Green Chem.*, 2012, **14**(6), 1611–1619, DOI: **10.1039/C2GC16619D**.

10 Neeraj Dhariwal, Vinod Kumar Meenu Chahar and O. P. Thakur, Ethanol sensing materials and device using Co^{2+}, Zn^{2+}, Cr^{2+} doped α-Fe_2O_3 nano-particles with room temperature response/recovery, *Sens. Actuators, B*, 2023, 134037, DOI: **10.1016/j.snb.2023.134037**.

11 H. Farahani, R. Wagiran and M. N. Hamidon, Humidity sensors principle, mechanism, and fabrication technologies: a comprehensive review, *Sensors*, 2014, **14**(5), 7881–7939, DOI: **10.3390/s140507881**.

12 S. Yu, H. Zhang, J. Zhang and Z. Li, Effects of pH on high-performance ZnO resistive humidity sensors using one-step synthesis, *Sensors*, 2019, **19**(23), 5267, DOI: **10.3390/s19235267**.

13 R. S. Dubey, S. Srilali, Y. T. Ravikiran, G. Satheesh Babu and K. V. Katta, Synthesis and characterization of $Zn_{x-1} Al_2 O_4$ $(TiO_2)_x$ nanocomposite ceramics and their humidity sensing properties, *J. Mater. Sci.*, 2022, 1–14, DOI: **10.1007/s10853-021-06709-0**.

14 B. Rohilla and S. Duhan, Modification of mesoporous SBA-16 with cobalt doping for outstanding humidity sensor at room temperature, *J. Porous Mater.*, 2023, 1–14, DOI: **10.1007/s10934-023-01499-z**.

15 A. Kumar, G. Gupta, K. Bapna and D. D. Shivagan, Semiconductor-metal-oxide-based nano-composites for humidity sensing applications, *Mater. Res. Bull.*, 2023, **158**, 112053, DOI: **10.1016/j.materresbull.2022.112053**.

16 E. Poonia, P. K. Mishra, V. Kiran, J. Sangwan, R. Kumar, P. K. Rai, R. Malik, V. K. Tomer, R. Ahuja and Y. K. Mishra, Aero-gel based CeO_2 nanoparticles: synthesis, structural properties and detailed humidity sensing response, *J. Mater. Chem. C*, 2019, **7**(18), 5477–5487, DOI: **10.1039/C9TC01081E**.

17 P. Malik, S. Sehrawat, A. Boora, B. Anisha, S. Kumari, Y. Ahlawat and S. Duhan, Optical and structural properties of Nd_2O_3-SiO_2 nanocomposite as synthesized from sol–gel technique, *Mater. Prot.*, 2023, **64**(4), 512–518, DOI: **10.5937/zasmat2304512M**.

18 J. Li, G. Xie, J. Jiang, Y. Liu, C. Chen, W. Li and J. Huang, Enhancing photodegradation of Methyl Orange by coupling piezo-phototronic effect and localized surface plasmon resonance, *Nano Energy*, 2023, **108**, 108234, DOI: **10.1016/j.nanoen.2023.108234**.

19 Q. Zhang, G. Xie, M. Duan, Y. Liu, Y. Cai, M. Xu, K. Zhao, H. Tai, Y. Jiang and Y. Su, Zinc oxide nanorods for light-activated gas sensing and photocatalytic applications, *ACS Appl. Nano Mater.*, 2023, **6**(19), 17445–17456, DOI: **10.1021/acsanm.3c02403**.

20 C. Chen, G. Xie, J. Dai, W. Li, Y. Cai, J. Li, Q. Zhang, H. Tai, Y. Jiang and Y. Su, Integrated core-shell structured smart textiles for active NO_2 concentration and pressure monitoring, *Nano Energy*, 2023, **116**, 108788, DOI: **10.1016/j.nanoen.2023.108788**.

21 Y. Li, W. Li, Z. Jin, X. Luo, G. Xie, H. Tai, Y. Jiang, Y. Yang and Y. Su, Ternary ordered assembled piezoelectric composite for self-powered ammonia detection, *Nano Energy*, 2024, **122**, 109291, DOI: **10.1016/j.nanoen.2024.109291**.

22 H. Pan, G. Chen, Y. Chen, A. Di Carlo, M. A. Mayer, S. Shen and C. Chen, Biodegradable cotton fiber-based piezoresistive textiles for wearable biomonitoring, *Biosens. Bioelectron.*, 2023, **222**, 114999, DOI: **10.1016/j.bios.2022.114999**.

23 Y. Su, W. Li, X. Cheng, Y. Zhou, S. Yang, X. Zhang and C. Chen, *et al.*, High-performance piezoelectric composites via β phase programming, *Nat. Commun.*, 2022, **13**(1), 4867, DOI: **10.1038/s41467-022-32518-3**.

24 N. M. Kiasari, S. Soltanian, B. Gholamkhass and P. Servati, Room temperature ultra-sensitive resistive humidity sensor based on single zinc oxide nanowire, *Sens. Actuators, A*, 2012, **182**, 101–105, DOI: **10.1016/j.sna.2012.05.041**.

25 S. Goktas and A. Goktas, A comparative study on recent progress in efficient ZnO based nanocomposite and heterojunction photocatalysts: A review, *J. Alloys Compd.*, 2021, **863**, 158734, DOI: **10.1016/j.jallcom.2021.158734**.

26 S. Peiris, H. B. de Silva, K. N. Ranasinghe, S. V. Bandara and I. R. Perera, Recent development and future prospects of TiO2 photocatalysis, *J. Chin. Chem. Soc.*, 2021, **68**(5), 738–769, DOI: **10.1002/jccs.202000465**.

27 S. Arora, V. Gosu and V. Subbaramaiah, One-pot synthesis of glycerol carbonate from glycerol using three-dimensional mesoporous silicates of K/TUD-1 under environmentally benign conditions, *Mol. Catal.*, 2020, **496**, 111188, DOI: **10.1016/j.mcat.2020.111188**.

28 Z. Shen, H. Zhou, H. Chen, H. Xu, C. Feng and X. Zhou, Synthesis of nano-zinc oxide loaded on mesoporous silica by coordination effect and its photocatalytic degradation property of methyl orange, *Nanomaterials*, 2018, **8**(5), 317, DOI: **10.3390/nano8050317**.

29 M. W. Ibrahim, M. A. Al-Obaidi, H. Kosslick and A. Schulz., Photocatalytic degradation of pharmaceutical pollutants using zinc oxide supported by mesoporous silica, *J. Sol–Gel Sci. Technol.*, 2021, **98**, 300–309, DOI: **10.1007/s10971-021-05507-z**.

30 M. F. Abdel Messih, A. E. Shalan, M. F. Sanad and M. A. Ahmed, Facile approach to prepare $ZnO@SiO_2$ nanomaterials for photocatalytic degradation of some organic pollutant models, *J. Mater. Sci.: Mater. Electron.*, 2019, **30**, 14291–14299, DOI: **10.1007/s10854-019-01798-9**.

31 V. Gupta, R. Malik and L. Kumar, Highly efficient and cost-effective polyaniline-based ammonia sensor on the biodegradable paper substrate at room temperature, *Mater. Chem. Phys.*, 2023, **310**, 128388, DOI: **10.1016/j.matchemphys.2023.128388**.

32 P. E. Boahene, S. Vedachalam and A. K. Dalai, Catalytic oxidative desulfurization of light gas oil over Keggin-type phosphomolybdic acid supported on TUD-1 metallosilicates, *Fuel*, 2022, **317**, 123447, DOI: **10.1016/j.fuel.2022.123447**.

33 S.-M. Jeong, A. Burri, N. Jiang and S.-E. Park, Microwave synthesis of hydrophobic Ti-TUD-1 mesoporous silica for catalytic oxidation of cycloolefins, *Appl. Catal., A*, 2014, **476**, 39–44, DOI: **10.1016/j.apcata.2014.02.008**.

34 P. Waller, Z. Shan, L. Marchese, G. Tartaglione, W. Zhou, J. C. Jansen and T. Maschmeyer, Zeolite nanocrystals inside mesoporous TUD-1: A high-performance catalytic composite, *Chem. – Eur. J.*, 2004, **10**(20), 4970–4976, DOI: **10.1002/chem.200400343**.

35 P. Bindu and S. Thomas, Estimation of lattice strain in ZnO nanoparticles: X-ray peak profile analysis., *J. Theor. Appl. Phys.*, 2014, **8**, 123–134, DOI: **10.1007/s40094-014-0141-9**.

36 M. S. Hamdy, B. M. Al-Shehri, K. S. Al-Namshah and M. Shkir, Synthesis, characterization, and photoluminescence property of Nd–TUD-1, *Luminescence*, 2021, **36**(1), 192–199, DOI: **10.1002/bio.3934**.

37 B. M. Al-Shehri, A.-R. Khder, S. S. Ashour, A. M. Alhanash, M. Shkir and M. S. Hamdy, Effect of europium loading on

the photoluminescence property of europium incorporated 3D-Mesoporous silica, *J. Non-Cryst. Solids*, 2019, **515**, 68–74, DOI: **10.1016/j.jnoncrysol.2019.04.007**.

38 S. Jakhar, S. Duhan and S. Nain, Novel one step hydrothermal synthesis of cubic Ia3d large pore 3D mesoporous In2O3/KIT-6 hybrid nanocomposite with humidity sensing applications, *J. Porous Mater.*, 2020, **27**(5), 1253–1263, DOI: **10.1007/s10934-020-00897-x**.

39 M. C. Moulton, L. K. Braydich-Stolle, M. N. Nadagouda, S. Kunzelman, S. M. Hussain and R. S. Varma, Synthesis, characterization and biocompatibility of ''green'' synthesized silver nanoparticles using tea polyphenols, *Nanoscale*, 2010, **2**(5), 763–770.

40 Y. K. Ooi, L. Yuliati and S. L. Lee, Phenol photocatalytic degradation over mesoporous TUD-1-supported chromium oxide-doped titania photocatalyst, *Chin. J. Catal.*, 2016, **37**(11), 1871–1881, DOI: **10.1016/S1872-2067(16)62492-0**.

41 B. M. Al-Shehri, S. K. Mohamed, S. Alzahly and M. S. Hamdy, A significant improvement in adsorption behavior of mesoporous TUD-1 silica through neodymium incorporation, *J. Rare Earths*, 2021, **39**(4), 469–476, DOI: **10.1016/j.jre.2020.07.004**.

42 S. Jakhar, S. Duhan and S. Nain, Facile hydrothermal synthesis of mesoporous WO3/KIT-6 nanocomposite depicting great humidity sensitive properties, *Mater. Res. Innovations*, 2022, **26**(4), 203–213, DOI: **10.1080/14328917.2021.1940668**.

43 I. Fatimah, G. Fadillah, I. Sahroni, A. Kamari, S. Sagadevan and R.-A. Doong, Nanoflower-like composites of ZnO/SiO2 synthesized using bamboo leaves ash as reusable photocatalyst, *Arabian J. Chem.*, 2021, **14**(3), 102973, DOI: **10.1016/j.arabjc.2020.102973**.

44 M. F. Abdel Messih, A. E. Shalan, M. F. Sanad and M. A. Ahmed, Facile approach to prepare ZnO@SiO2 nanomaterials for photocatalytic degradation of some organic pollutant models, *J. Mater. Sci.: Mater. Electron.*, 2019, **30**, 14291–14299, DOI: **10.1007/s10854-019-01798-9**.

45 M. V. Arularasu, M. Harb, R. Vignesh, T. V. Rajendran and R. Sundaram, PVDF/ZnO hybrid nanocomposite applied as a resistive humidity sensor, *Surf. Interfaces*, 2020, **21**, 100780, DOI: **10.1016/j.surfin.2020.100780**.

46 S. Yu, H. Zhang, J. Zhang and Z. Li, Effects of pH on high-performance ZnO resistive humidity sensors using one-step synthesis, *Sensors*, 2019, **19**(23), 5267, DOI: **10.3390/s19235267**.

47 R. Akram, M. Saleem, Z. Farooq, M. Yaseen, Z. M. Almohaimeed and Q. Zafar, Integrated Capacitive-and Resistive-Type Bimodal Relative Humidity Sensor Based on 5,10,15,20-Tetraphenylporphyrinatonickel(ɪɪ) (TPPNi) and Zinc Oxide (ZnO) Nanocomposite, *ACS omega*, 2022, **7**(34), 30590–30600, DOI: **10.1021/acsomega.2c04313**.

48 B. Tao, J. Yin, F. Miao and Y. Zang, High-performance humidity sensor based on GO/ZnO/plant cellulose film for respiratory monitoring, *Ionics*, 2022, **28**(5), 2413–2421, DOI: **10.1007/s11581-022-04478-7**.

49 P. Li and F. Yang, Preparation and performance of TiO2/ZnO humidity sensor based on TiO2, *J. Mater. Sci. Eng. B*, 2023, **298**, 116902, DOI: **10.1016/j.mseb.2023.116902**.

50 M. A. Dwiputra, F. Fadhila, C. Imawan and V. Fauzia, The enhanced performance of capacitive-type humidity sensors based on ZnO nanorods/WS2 nanosheets heterostructure, *Sens. Actuators, B*, 2020, **310**, 127810, DOI: **10.1016/j.snb.2020.127810**.

51 S. Yu, H. Zhang, C. Chen and C. Lin, Investigation of humidity sensor based on Au modified ZnO nanosheets via hydrothermal method and first principle, *Sens. Actuators, B*, 2019, **287**, 526–534, DOI: **10.1016/j.snb.2019.02.089**.

52 A. K. Khaleel and L. K. Abbas, Synthesis and characterization of PVDF/PMMA/ZnO hybrid nanocomposite thin films for humidity sensor application, *Optik*, 2023, **272**, 170288, DOI: **10.1016/j.ijleo.2022.170288**.

53 H. Parangusan, J. Bhadra, Z. Ahmad, S. Mallick, F. Touati and N. Al-Thani, Humidity sensor based on poly (lactic acid)/PANI–ZnO composite electrospun fibers, *RSC Adv.*, 2021, **11**(46), 28735–28743, DOI: **10.1039/D1RA02842A.**

54 E. M. Rodriguez, G. Marquez, M. Tena, P. M. Álvarez and F. J. Beltrán, Determination of main species involved in the first steps of TiO2 photocatalytic degradation of organics with the use of scavengers: The case of ofloxacin, *Appl. Catal., B*, 2015, **178**, 44–53, DOI: **10.1016/j.apcatb.2014.11.002**.

55 K. Doudrick, T. Yang, K. Hristovski and P. Westerhoff, Photocatalytic nitrate reduction in water: Managing the hole scavenger and reaction by-product selectivity, *Appl. Catal., B*, 2013, **136**, 40–47, DOI: **10.1016/j.apcatb.2013.01.042**.

56 T. Tan, D. Beydoun and R. Amal, Effects of organic hole scavengers on the photocatalytic reduction of selenium anions, *J. Photochem. Photobiol. A: Chem.*, 2003, **159**(3), 273–280, DOI: **10.1016/S1010-6030(03)00171-0**.

57 N. Agmon, The grotthuss mechanism, *Chem. Phys. Lett.*, 1995, **244**(5–6), 456–462, DOI: **10.1016/0009-2614(95)00905-J**.

58 S. A. Fischer and D. Gunlycke, Analysis of correlated dynamics in the Grotthuss mechanism of proton diffusion, *J. Phys. Chem. B*, 2019, **123**(26), 5536–5544, DOI: **10.1021/acs.jpcb.9b02610**.

59 M. Zakertabrizi, E. Hosseini, A. H. Korayem, A. Razmjou, A. G. Fane and V. Chen, Insight from perfectly selective and ultrafast proton transport through anhydrous asymmetrical graphene oxide membranes under Grotthuss mechanism, *J. Membr. Sci.*, 2021, **618**, 118735, DOI: **10.1016/j.memsci.2020.118735**.

60 M. V. Arularasu, M. Harb, R. Vignesh, T. V. Rajendran and R. Sundaram, PVDF/ZnO hybrid nanocomposite applied as a resistive humidity sensor, *Surf. Interfaces*, 2020, **21**, 100780, DOI: **10.1016/j.surfin.2020.100780**.